

# Interactions between Ultrastable $\text{Na}_4\text{Ag}_{44}(\text{SR})_{30}$ Nanoclusters and Coordinating Solvents: Uncovering the Atomic-scale Mechanism

*Daniel M. Chevrier,<sup>1,†</sup> Brian E. Conn,<sup>2</sup> Bo Li,<sup>3</sup> De-en Jiang,<sup>3</sup> Terry P. Bigioni,<sup>2</sup> Amares Chatt,<sup>1</sup> Peng Zhang<sup>\*1</sup>*

<sup>1</sup>Department of Chemistry, Dalhousie University, Halifax, NS B3H 4J3, Canada

<sup>2</sup>Department of Chemistry and Biochemistry, University of Toledo, Toledo, Ohio 43606, United States

<sup>3</sup>Department of Chemistry, University of California, Riverside, California 92521, United States

\*Corresponding Author: peng.zhang@dal.ca

**ABSTRACT:** Recently, silver nanoclusters have garnered considerable attention after the high-yield synthesis and crystallization of a thiolate-protected silver nanocluster,  $\text{Na}_4\text{Ag}_{44}(\text{SR})_{30}$  (SR – protecting thiolate ligand). One intriguing feature of  $\text{Na}_4\text{Ag}_{44}(\text{SR})_{30}$  is its outstanding stability and resistance to chemical reactions, in striking difference from other silver nanostructures whose susceptibility to oxidation (tarnishing) has been commonly observed and thus limits their applications in nanotechnology. Herein, we report the mechanism on the ultrahigh stability of  $\text{Na}_4\text{Ag}_{44}(\text{SR})_{30}$  by uncovering how coordinating solvents interact with the  $\text{Na}_4\text{Ag}_{44}(\text{SR})_{30}$  nanocluster at the atomic scale. Through synchrotron X-ray experiments and theoretical calculations, it was found that strongly coordinating aprotic solvents interact with surface Ag atoms, particularly between ligand bundles, which compresses the Ag core and relaxes surface metal-ligand interactions. Furthermore, water was used as a cosolvent to demonstrate that semi-aqueous conditions play an important role in protecting exposed surface regions and can further influence the local structure of the silver nanocluster itself. Notably, under semi-aqueous conditions, aprotic coordinating solvent molecules preferentially remain on the metal surface while water molecules interact with ligands, and ligand bundling persisted across the varied solvation conditions. This work offers an atomic level mechanism on the ultrahigh stability of the  $\text{Na}_4\text{Ag}_{44}(\text{SR})_{30}$  nanoclusters from the nanocluster-coordinating solvent interaction perspective, and implies that nanocluster-solvent interactions should be carefully considered moving forward for silver nanoclusters, as they can influence the electronic/chemical properties of the nanocluster as well as the surface accessibility of small molecules for potential catalytic and biomedical applications.

**KEYWORDS:** Thiolate-silver nanocluster, Coordinating solvents, Cluster-solvent interactions, X-ray absorption spectroscopy, Quantum mechanical/molecular mechanical calculations, Nanocluster stability, Local structure

Thiolate-protected silver nanoparticles (Ag NPs) and smaller (1-3 nm diameter) nanoclusters (Ag NCs) have been investigated for several years alongside the ground-breaking progress made with thiolate-protected Au NPs and NCs.<sup>1-4</sup> After the leap forward from elucidating the thiolate-protected Au NC structure and properties (*i.e.*, crystallization of Au<sub>102</sub>),<sup>5</sup> progress in Ag NC analogs soon followed. Ag-based NPs and NCs are an enticing alternative since Ag is not as precious as Au and offers another suite of chemical and physical properties employable for application. For example, the antibacterial properties of Ag can be utilized for biomedical applications and the superior optical properties of Ag-based NPs have shown potential as advanced light harvesting materials.<sup>6,7</sup> Importantly, the lower cost of Ag is beneficial for scaling up syntheses toward cost-effective production for application or industrial utilization. Despite these advantages, Ag NPs have been known to suffer from tarnishing,<sup>8</sup> which affects Ag NP stability and long-term usage of these materials in application stages or on an industrial scale. This problem also interferes with the fundamental characterization and understanding of optical and electronic properties as they relate to the size, structure and surface environment of Ag NPs and NCs.

More recently, thiolate-protected Ag NCs have made significant progresses in the field of atomically precise nanoclusters. Advances in metal NC synthesis techniques have enabled the preparation and isolation of not only new Ag NC species, but a few Ag<sub>n</sub>(SR)<sub>m</sub> NCs (where n and m are integers, SR – is the protecting thiolate ligand).<sup>9,10</sup> Notably, structural elucidation of M<sub>4</sub>Ag<sub>44</sub>(SR)<sub>30</sub> NCs (M – charge counterbalancing metal cation) was a significant discovery for the metal NC community.<sup>11,12</sup> The crystal structures revealed a distinctive metal core with discrete Ag-SR surface structural units, much like the general construction of thiolate-protected Au NCs. The exceptional stability of M<sub>4</sub>Ag<sub>44</sub>(SR)<sub>30</sub> is unprecedented for Ag NPs and NCs. The M<sub>4</sub>Ag<sub>44</sub>(SR)<sub>30</sub> structure is so greatly favored over other Ag NC structures that single-species M<sub>4</sub>Ag<sub>44</sub>(SR)<sub>30</sub> products are attainable in quantitative yields, and the reaction can be scaled up to produce over 100 g of M<sub>4</sub>Ag<sub>44</sub>(SR)<sub>30</sub> NCs per batch.<sup>12,13</sup> Other properties of interest for M<sub>4</sub>Ag<sub>44</sub>(SR)<sub>30</sub> NCs include a rich, broadband light absorption across the UV-Vis spectrum, moderate photoluminescence, and catalytic activity.<sup>13-15</sup>

The exceptional stability of  $M_4Ag_{44}(SR)_{30}$  has been attributed to the closed atomic shell structure of the  $Ag_{32}$  core ( $Ag_{12}$  icosahedron inside  $Ag_{20}$  dodecahedron), the closed electronic shell structure of the molecule ( $1S^2|1P^6|1D^{10}$ , following the Aufbau rule), and the choice of protecting ligands.<sup>11,12</sup> It was also recognized that coordinating solvents played a key role in the stabilization of  $M_4Ag_{44}(p-MBA)_{30}$  ( $p-MBA$  = *para*-mercaptobenzoic acid), although the mechanism was not fully understood.<sup>12,13</sup> Further, it was demonstrated that increasing the coordination strength of the solvent during synthesis increased the yield of  $M_4Ag_{44}(p-MBA)_{30}$ .<sup>13</sup>

Ligand shells are often thought of as isotropic coatings that offer uniform protection; however, this is generally not the case. Intramolecular interactions between ligands in the protective outer shell are known to result in the bundling of ligands, which can impart a more complex structure to the ligand shell.<sup>16,17</sup> In the case of  $Na_4Ag_{44}(p-MBA)_{30}$ , the  $p-MBA$  ligands were observed to form dimer and trimer bundles through  $\pi$ - $\pi$  (face-to-face) and C-H--- $\pi$  (edge-to-face) interactions between benzene rings, respectively, in the X-ray determined crystal structure.<sup>12</sup> Surprisingly, ligand bundling was also observed in NMR measurements of fully solvated molecules, suggesting that these intramolecular interactions are strong enough for the gaps in the ligand shell structure to persist in solution.<sup>13</sup>

It has been recognized that the gaps created by ligand bundling in  $Na_4Ag_{44}(p-MBA)_{30}$  leave some of the Ag atoms unprotected and consequently exposed to potential chemical attack. It was therefore postulated that coordinating solvent molecules could protect the exposed Ag atoms, effectively forming a second shell of steric protection.<sup>12,13</sup> Such a secondary protective layer was not directly observed in single crystal X-ray diffraction measurements, however, presumably due to the mobility of the coordinating solvent molecules within the solvent-containing cavities of  $Na_4Ag_{44}(p-MBA)_{30}$  crystals. It therefore remains an open question as to the role of coordinating solvent molecules and the nature of their interactions with surface structures in the stability of  $Na_4Ag_{44}(p-MBA)_{30}$  as well as other related NCs.

With ligand shell and surface-based interactions recently generating significant interest,<sup>18–21</sup> there is a growing need for more detailed information on solvent effects on metal NC structure and surface

chemistry. Toward this end, the interactions between  $M_4Ag_{44}(SR)_{30}$  NCs and selected coordinating solvents were examined using synchrotron X-ray absorption fine structure (XAFS) spectroscopy and quantum mechanical / molecular mechanical (QM/MM) calculations to understand how coordinating solvent molecules interact and affect the local structure and bonding properties of  $M_4Ag_{44}(SR)_{30}$ . We demonstrate that the response of  $Na_4Ag_{44}(p-MBA)_{30}$  NCs to solvation interactions is measurable and provides atomic scale insight into how coordinating solvents stabilize the surface between ligand bundles and in turn affect the structure and properties of  $M_4Ag_{44}(SR)_{30}$ . Furthermore, this work demonstrates the utility of combining synchrotron X-ray experiments and computational chemistry for examining the surface chemistry of atomically precise metal NCs in solution.

## RESULTS AND DISCUSSION

### *Site-specific analysis on the core and surface bonding environments*

The crystal structure of  $Na_4Ag_{44}(p-MBA)_{30}$  (Figure 1a-d) has a compact  $Ag_{32}$  core that is composed of a hollow  $Ag_{12}$  icosahedron inside of a  $Ag_{20}$  dodecahedron. Protecting the  $Ag_{32}$  core are six  $Ag_2(p-MBA)_5$  capping units known as “mount” motifs, which are positioned in an octahedral geometry around the  $Ag_{32}$  core. Bundles of two and three ligands can be seen on each mount, which result from the intramolecular  $\pi$ - $\pi$  and C-H--- $\pi$  interactions between *p*-MBA ligands (Figure 1d). This organization of ligands exposes the 12 Ag atoms in the 6 mounts as well as 8 Ag atoms at the feet of the mounts in the dodecahedral shell.<sup>22</sup>

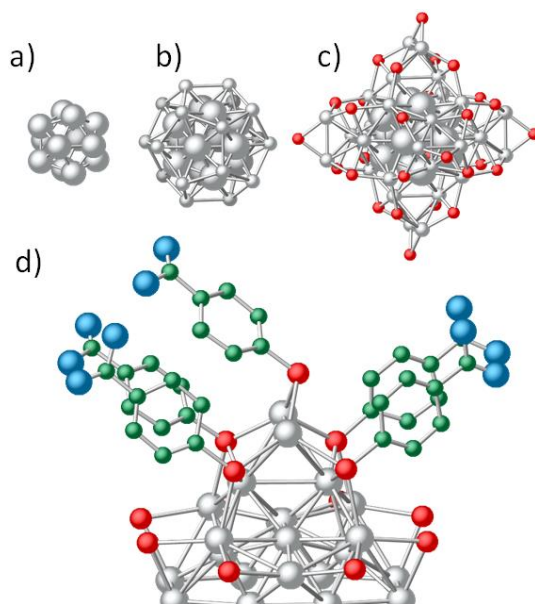


**Figure 1.**  $\text{Na}_4\text{Ag}_{44}(\text{p-MBA})_{30}$  structure from center to surface: a) hollow  $\text{Ag}_{12}$  icosahedron to b)  $\text{Ag}_{20}$  dodecahedron to c) six  $\text{Ag}_2\text{S}_5$  mounts (silver – Ag, red – S). The organic portion of the protecting ligands is removed for clarity. d) Mount structures on the cluster surface (blue – O, green – C) illustrating ligand bundling and open clefts (H atoms removed for clarity).

From inspection of the Ag-Ag and Ag-S bond length distributions in the crystal structure (Figure 2a), three distinct environments were identified as EXAFS scattering shells for fitting analysis. The Ag-S shell corresponds to covalent bonding between thiolate ligands and Ag sites in the  $\text{Ag}_{20}$  cage and in the mounts (Figure 1c). The shorter distance Ag-Ag shell ( $\text{Ag-Ag}_1$ ) corresponds to bonding within the hollow  $\text{Ag}_{12}$  icosahedron as well as bonding between  $\text{Ag}_{12}$  and the  $\text{Ag}_{20}$  cage (Figure 1a-b). The third shell,  $\text{Ag-Ag}_2$ , represents Ag-Ag bonding at a longer distance, namely between the two Ag atoms in the mounts, between Ag atoms within the  $\text{Ag}_{20}$  cage, and between mount and cage Ag sites.

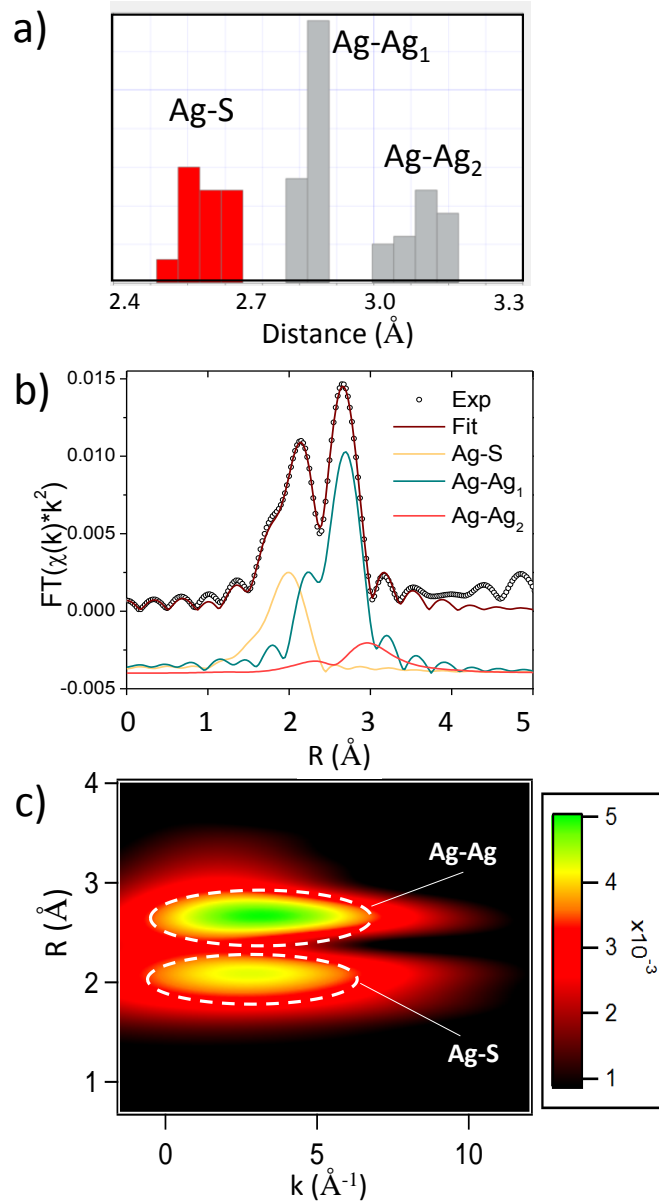


**Figure 2.** a) Bond length distribution histogram of Na<sub>4</sub>Ag<sub>44</sub>(*p*-MBA)<sub>30</sub> with assigned EXAFS scattering paths. b) Ag K-edge FT-EXAFS at 90 K in the solid-phase, showing total fit and individual contributions from each scattering path. c) Wavelet-transformed EXAFS map showing two domains corresponding to the Ag-S shell and Ag-Ag shells (*i.e.*, the Ag-Ag<sub>1</sub> and Ag-Ag<sub>2</sub> shells are overlapping in the 2D map).

In order to verify the reliability of the EXAFS fitting protocol to be used in this work, Ag K-edge EXAFS of Na<sub>4</sub>Ag<sub>44</sub>(*p*-MBA)<sub>30</sub> in the solid-phase at 90 K was first analyzed using the Ag-S and Ag-Ag scattering shells described above; the fit is shown in Figure 2b and fitted parameters are given in Table 1. Fitted Ag-

S and Ag-Ag bond distances matched well with the average bond lengths determined from the crystal structure that was also obtained at low temperature ( $R_{\text{Ag-S}} = 2.55 \text{ \AA}$ ,  $R_{\text{Ag-Ag1}} = 2.84 \text{ \AA}$ ,  $R_{\text{Ag-Ag2}} = 3.14 \text{ \AA}$ ), proving the suitability of the designated EXAFS scattering shells to account for, and

**Table 1.** EXAFS fitting results for  $\text{Na}_4\text{Ag}_{44}(\text{p-MBA})_{30}$  at 90 K in the solid-phase. Uncertainties in fitted parameters are shown in parentheses; Debye–Waller factor ( $\sigma^2$ ); energy-shift parameter ( $\Delta E_0$ ).

Shell	CN	R ( $\text{\AA}$ )	$\sigma^2$ ( $\text{\AA}^2$ )	$\Delta E_0$ (eV)
Ag-S	1.9	2.501(7)	0.0066(4)	1(1)
Ag-Ag <sub>1</sub>	4.1	2.876(3)	0.0051(1)	2.0(4)
Ag-Ag <sub>2</sub>	3.3	3.08(1)	0.021(3)	2.0(4)

distinguish, core and surface interactions. Complementary to FT-EXAFS, a wavelet-transformed EXAFS (WT-EXAFS) was obtained to analyze the local structure from a two-dimensional (2D) mapping perspective (Figure 2c, Figure S1). This 2D mapping approach is used in the following sections to illustrate the sensitive local structural change of the NCs (*i.e.*, the Ag-S and Ag-Ag domains) induced by various cluster-solvent interactions.

#### *Coordinating aprotic solvent molecules interact directly with the nanocluster surface*

In order to study the interactions between  $\text{Na}_4\text{Ag}_{44}(\text{p-MBA})_{30}$  and coordinating solvents, solid- and solution-phase XAFS measurements using DMF and DMSO solvents were first conducted at 300 K ( $k$ -space spectra shown in Figure S2). The EXAFS spectra were fitted for each condition using the three scattering shells described in Figure 1b and are shown in Figure S3 with associated fitting results in Table 2. We note that the near-edge structure (Figure S4) varies little across the series of  $\text{Na}_4\text{Ag}_{44}(\text{p-MBA})_{30}$  measurements, which is due to the similar final valence states in the dipole-allowed transition from  $1s \rightarrow 5p$  as seen for Ag K-edge transitions.



EXAFS fitting results for  $\text{Na}_4\text{Ag}_{44}(\text{p-MBA})_{30}$  at 300 K in the solid-phase were consistent with results from 90 K, but with small variations in average bond distances and, as expected, higher Debye-Waller factors from thermal disorder. Notably, Ag-S and surface Ag-Ag ( $\text{Ag-Ag}_2$ ) bond distances did not change significantly with temperature whereas Ag-Ag bonds related to the  $\text{Ag}_{32}$  core ( $\text{Ag-Ag}_1$ ) decreased in length. The solid-phase temperature comparison may demonstrate a rigid surface layer while the hollow  $\text{Ag}_{12}$  core is more susceptible to thermal vibrations and fluctuations.

**Table 2.** EXAFS fitting results for  $\text{Na}_4\text{Ag}_{44}(\text{p-MBA})_{30}$  NCs in solid-phase and in solution-phase conditions (DMF and DMSO) at 300 K. Uncertainties in fitted parameter are shown in parentheses; Debye–Waller factor ( $\sigma^2$ ); energy-shift parameter ( $\Delta E_0$ ).

Condition	Shell	CN	R (Å)	$\sigma^2$ (Å <sup>2</sup> )	$\Delta E_0$ (eV)
Solid	Ag-S	1.9	2.50(1)	0.011(1)	0(1)
	Ag-Ag <sub>1</sub>	4.1	2.83(1)	0.013(1)	0(1)
	Ag-Ag <sub>2</sub>	3.3	3.09(5)	0.03(1)	0(1)
DMF	Ag-S	1.9	2.525(7)	0.010(6)	-2.0(6)
	Ag-Ag <sub>1</sub>	4.1	2.816(5)	0.011(4)	-2.0(6)
	Ag-Ag <sub>2</sub>	3.3	3.02(2)	0.031(6)	-2.0(6)
DMSO	Ag-S	1.9	2.52(1)	0.010(9)	-1.4(8)
	Ag-Ag <sub>1</sub>	4.1	2.818(8)	0.012(7)	-1.4(8)
	Ag-Ag <sub>2</sub>	3.3	3.04(3)	0.025(6)	-1.4(8)

DMSO and DMF were selected as coordinating solvents based on the documented preparation of  $\text{Na}_4\text{Ag}_{44}(\text{p-MBA})_{30}$  NCs.<sup>12</sup>  $\text{Na}_4\text{Ag}_{44}(\text{p-MBA})_{30}$  NCs in DMF or DMSO had similar structural responses to solvation when comparing the fitted parameters with the solid-phase EXAFS measurements (fitting results in Table 2). The average Ag-S bond length increased by ~0.02 Å when dissolved in DMF or DMSO and the associated Debye-Waller factor remained similar to the solid-phase. Exterior Ag-Ag interactions ( $\text{Ag-Ag}_2$ ) markedly decreased in average distance for  $\text{Na}_4\text{Ag}_{44}(\text{p-MBA})_{30}$  in solution, while the interior

Ag-Ag bonding within the Ag<sub>32</sub> core (Ag-Ag<sub>1</sub>) decreased only slightly in distance and disorder. These structural changes associated with the nanocluster-solvent interactions are further supported by WT-EXAFS results shown in Figure 3. As can be directly seen in the 2D maps, the DMF and DMSO solvated NCs both show clear changes in intensity of the Ag-S and Ag-Ag domains when compared with the solid-phase sample. Such changes can be attributed to less thermally induced disorder in Ag local structure of Na<sub>4</sub>Ag<sub>44</sub>(*p*-MBA)<sub>30</sub> in solution-phase, which would increase the EXAFS oscillation signal originating from Ag-S and Ag-Ag bonding. In addition, the WT-EXAFS maps of these two solvated NCs are similar, indicating that the two solvents interact with Na<sub>4</sub>Ag<sub>44</sub>(*p*-MBA)<sub>30</sub> in a similar manner.

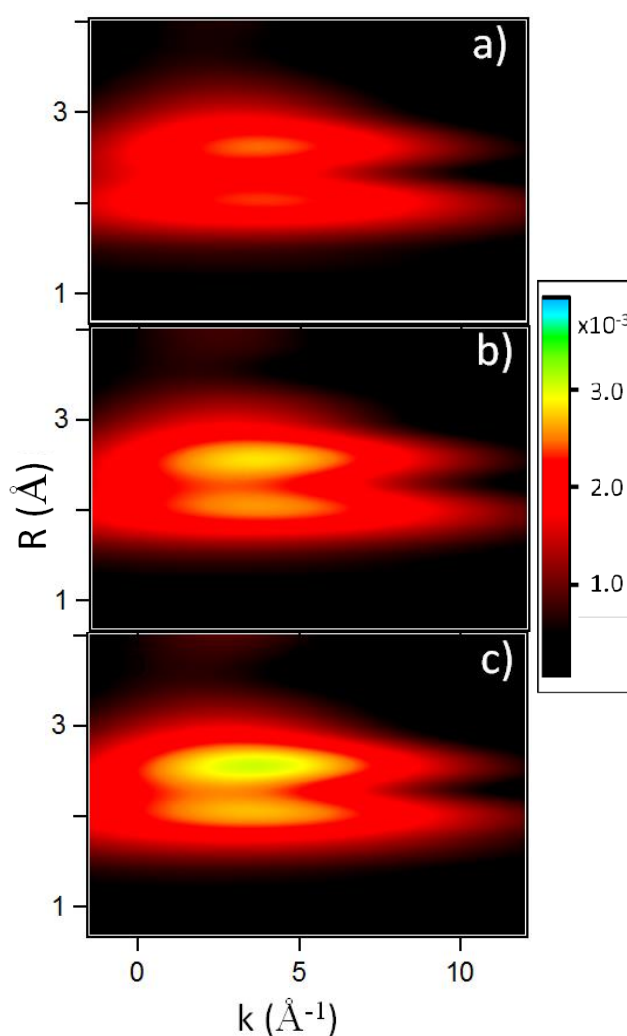


**Figure 3.** Wavelet-transformed EXAFS 2D maps showing the visible changes of the Ag-S and Ag-Ag domains when Na<sub>4</sub>Ag<sub>44</sub>(*p*-MBA)<sub>30</sub> is measured in a) solid phase, b) DMF solution and c) DMSO solution.

S K-edge XANES measurements (Figure 4) provide a complimentary perspective and reveal that electronic properties of the S atoms change when dissolved in solution (only DMF was measured since the sulfoxide moiety in DMSO interferes with this measurement). The most intense peak for  $\text{Na}_4\text{Ag}_{44}(p\text{-MBA})_{30}$  following the absorption edge, commonly known as the white-line, was broadened compared to free thiol ligands due to S-Ag interactions. The white-line intensity for  $\text{Na}_4\text{Ag}_{44}(p\text{-MBA})_{30}$  in DMF was higher than the solid-phase, which could be due to redistribution of electron orbital density in S as a result of solvent interactions with the *p*-MBA ligands or Ag NC core. This shift in electron density from the S atoms to the Ag NC core would be consistent with core contraction under solvation.

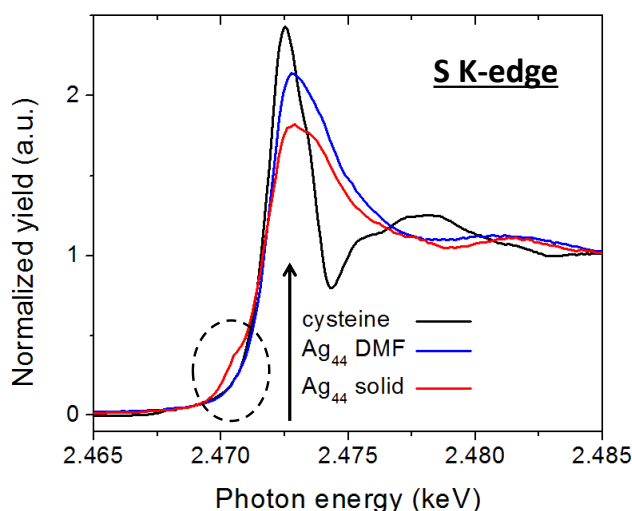


**Figure 4.** Sulfur K-edge XANES of thiol reference (cysteine), solid-phase  $\text{Na}_4\text{Ag}_{44}(p\text{-MBA})_{30}$  and  $\text{Na}_4\text{Ag}_{44}(p\text{-MBA})_{30}$  in DMF.

Disappearance of the pre-edge feature (dashed circle in Figure 4) for  $\text{Na}_4\text{Ag}_{44}(p\text{-MBA})_{30}$  upon dissolution of the Ag NCs into DMF is interesting to note. The origin of this feature has been described as the antibonding state of metal-sulfur interaction involving both s and p character of S and has been observed to be more prominent with a higher contribution of metal-metal bonding (*i.e.*, larger metal core and mixing of metal atom states), but also when there are vacancies in the LUMO states for the bound metal species.<sup>23,24</sup> Since there is no compositional change of  $\text{Na}_4\text{Ag}_{44}(p\text{-MBA})_{30}$  in solution, the obvious change

of this spectral feature in Figure 4 indicates that the solvation-induced local structural change resulted in a considerable variation of the S-Ag bonding properties from the S perspective.

To pinpoint and further confirm the contracting Ag NC core framework and the potential change in electronic properties of S and Ag from solvent interactions, QM/MM simulations were conducted on a  $\text{Na}_4\text{Ag}_{44}(\text{p-MBA})_{30}$  cluster surrounded by DMSO molecules. QM treatment was given to the  $\text{Na}_4\text{Ag}_{44}(\text{p-MBA})_{30}$  cluster and its first solvation shell while MM was used for the surrounding solvent environment. It can be seen from a simulation with DMSO molecules (Figure 5a) that the coordinating solvent occupies regions between ligand bundles, from the carboxylic acid ends of *p*-MBA to the Ag NC surface. From integrating the radial distribution function and inspection, it seems about 3-4 DMSO molecules are within 3-4 Angstroms of the surface Ag for each nanocluster. The closest average radial distance of the

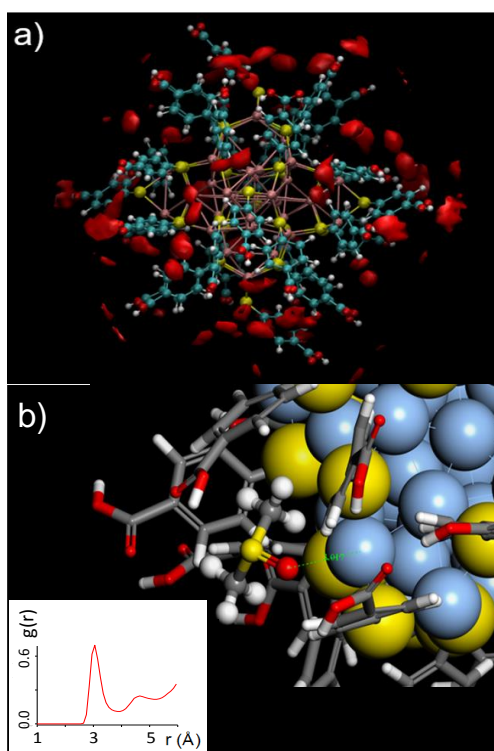


**Figure 5.** a) QM/MM simulations of DMSO (red clouds) distribution around  $\text{Na}_4\text{Ag}_{44}(\text{p-MBA})_{30}$  (pink – Ag, yellow – S, cyan – C, red – O, white - H). b) Interactions between DMSO molecules and surface Ag sites QM/MM simulations (inset: radial distribution plot of sulfoxide distances to Ag on NC surface)

coordinating sulfoxide group to Ag atoms on the surface was found to be  $\sim 3.0$  Å (Figure 5b inset), which is short enough for considerable electronic interactions (e.g. electron donation from oxygen lone-pair electrons to surface Ag which carries partial positive charge). The sulfoxide distance to S atoms of thiolate ligands is on average slightly longer at  $\sim 4.0$  Å (Figure S5). Together, these results indicate that the positions of the DMSO around the nanocluster is not random, where DMSO has a preference for positions nearer to Ag surface atoms. Combining the proximity of DMSO molecules to the Ag NC surface from simulation and experimental results of contracted Ag NC core, and the change in S electronic properties, it is evident that an electronic interaction between solvent and the Ag NC surface could account for these observations. It is further noted that ligand bundling persisted after the addition of DMSO in the simulation.

Compared to our previous studies of  $\text{Au}_n(\text{SR})_m$  NCs in solution,<sup>21,25</sup> less surface structural disorder was detected for  $\text{Na}_4\text{Ag}_{44}(\text{p-MBA})_{30}$  NCs in solution. This is likely because thiolate ligands on the measured Au NCs are not expected to form distinct ligand bundles. The observation of solution-phase ligand bundling on  $\text{Na}_4\text{Ag}_{44}(\text{p-MBA})_{30}$  NCs by NMR as well as our QM/MM simulations here suggest that ligand-ligand interactions are strong enough to enable ligand bundling to persist in dynamic environments. This solution-phase bundling creates opportunities for significant interactions between solvent molecules and Ag atoms on the surface, rather than only solvent-ligand interactions. Carboxylic acid groups may also play a role in ligand bundling and may interact with water molecules through hydrogen bonding to further stabilize ligand bundles. Therefore, based on solution-induced changes of Ag-S and Ag-Ag bonding from EXAFS, solution-phase ligand bundling observed by NMR and QM/MM, and requirement of coordinating solvents in the synthesis of  $\text{Na}_4\text{Ag}_{44}(\text{p-MBA})_{30}$  NCs, the coordination interaction of DMSO and DMF solvents clearly contribute to the overall stability of  $\text{Na}_4\text{Ag}_{44}(\text{p-MBA})_{30}$ .

*Water as a co-solvent interacts with ligands and surface, relaxing the Ag NC core*

The final consideration is how nanocluster-solvent interactions and nanocluster local structure itself can be further tailored by controlling solution conditions. Based on the semi-aqueous reaction conditions

reported for the synthesis and our observation of DMSO interacting with the surface Ag, we tested the structural response of  $\text{Na}_4\text{Ag}_{44}(\text{p-MBA})_{30}$  to solution-phase conditions where water was added as a co-solvent. Two solvent mixtures of DMSO (coordinating with the Ag NC surface) and water (interacting with carboxylate groups) were tested: 25% (v/v) DMSO/ $\text{H}_2\text{O}$  and 10% (v/v) DMSO/ $\text{H}_2\text{O}$ . Below 10% (v/v) DMSO/ $\text{H}_2\text{O}$ , solutions were no longer stable enough for XAFS measurement. However, the dissolution of  $\text{Na}_4\text{Ag}_{44}(\text{p-MBA})_{30}$  in such a high fraction of water could have been due to the neutral pH of the solution, whereas creating slightly more alkaline conditions would render *p*-MBA-protected clusters more soluble.<sup>26</sup>

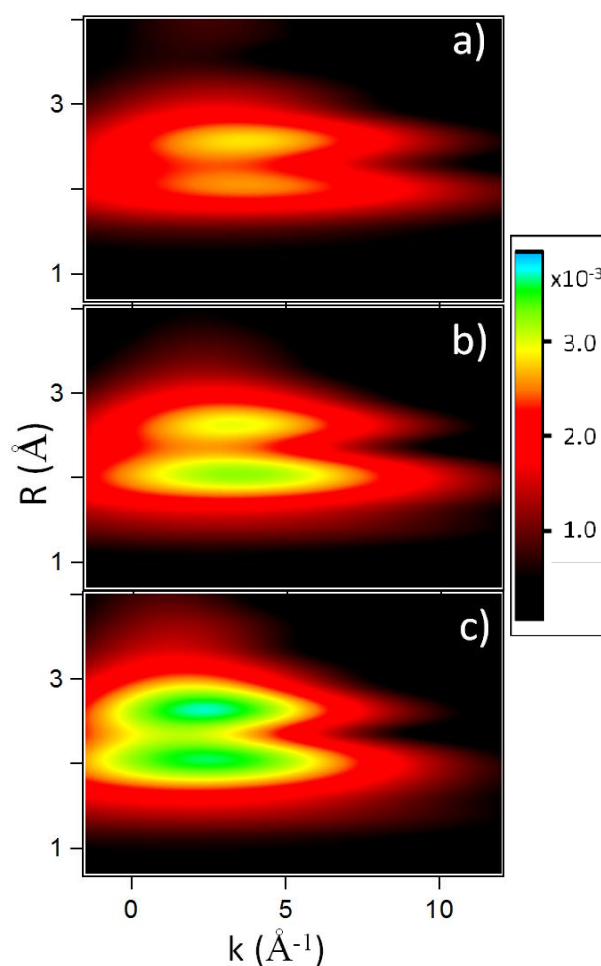


**Figure 6.** Wavelet-transformed EXAFS 2D maps showing the visible changes of the Ag-S and Ag-Ag domains for  $\text{Na}_4\text{Ag}_{44}(\text{p-MBA})_{30}$  in a) 100% DMSO, b) 25% DMSO and c) 10% DMSO.

To visually demonstrate the structural change induced by the co-solvent addition, WT-EXAFS 2D maps of  $\text{Na}_4\text{Ag}_{44}(\text{p-MBA})_{30}$  in 100%, 25% and 10% DMSO are shown in Figure 6. Both solvent mixtures show considerable changes in the WT-EXAFS Ag-S and Ag-Ag domains. As the concentration of DMSO decreases more pronounced changes occur to the shape and intensity of both Ag-S and Ag-Ag interactions in the WT-EXAFS plots. As expected, the 10% DMSO sample demonstrates the biggest changes in the WT-EXAFS features. Interestingly, the relative intensity of Ag-S and Ag-Ag domains shifts once water is added. Without water, the Ag-S domain in WT-EXAFS is less intense, but its relative intensity clearly increases with water added, suggesting the addition of water causes considerable change to the ligand-metal interactions. These observations are consistent with the EXAFS fitting results (Table 3). When water is added, Ag-S bonds shorten up to  $\sim 0.04 \text{ \AA}$  and metallic Ag-Ag bonds in the Ag NC core ( $\text{Ag-Ag}_1$ ) lengthen by  $\sim 0.04 \text{ \AA}$  compared to pure DMSO. For the case where the Ag-S bond length shrinks after adding water to the solvent mixture, we expect a combination of geometrical constraints from  $\text{H}_2\text{O-COOH}$  hydrogen bonding at the tails of p-MBA and a change in dielectric constant with a higher fraction of water over DMSO could favor more orbital overlap between Ag-S, thereby shortening the average bond length.

**Table 3.** EXAFS fitting results for  $\text{Na}_4\text{Ag}_{44}(\text{p-MBA})_{30}$  NCs in DMSO with water co-solvent at 300 K. Uncertainties in fitted parameter are shown in parentheses; Debye–Waller factor ( $\sigma^2$ ); energy-shift parameter ( $\Delta E_0$ ).

Condition	Shell	CN	R ( $\text{\AA}$ )	$\sigma^2$ ( $\text{\AA}^2$ )	$\Delta E_0$ (eV)
DMSO	Ag-S	1.9	2.52(1)	0.010(9)	-1.4(8)
	Ag-Ag <sub>1</sub>	4.1	2.818(8)	0.012(7)	-1.4(8)
	Ag-Ag <sub>2</sub>	3.3	3.04(3)	0.025(6)	-1.4(8)
25% DMSO	Ag-S	1.9	2.49(1)	0.0083(6)	-3(1)
	Ag-Ag <sub>1</sub>	4.1	2.863(8)	0.0123(7)	1.7(9)
	Ag-Ag <sub>2</sub>	3.3	3.07(2)	0.023(4)	1.7(9)
10% DMSO	Ag-S	1.9	2.479(9)	0.0097(4)	-2(1)
	Ag-Ag <sub>1</sub>	4.1	2.854(5)	0.0114(4)	2.1(5)
	Ag-Ag <sub>2</sub>	3.3	3.05(1)	0.020(2)	2.1(5)

No increase in surface or core bond disorder was detected for Ag-Ag interactions based on the fitted Debye-Waller factors. The fitting uncertainty associated with the Debye-Waller factor for Ag-S distances decreased from 90% to 4-7% when going from DMSO to DMSO/H<sub>2</sub>O solvents. The change in Ag-S bond length and reduction in fitting uncertainty suggest that the combination of aprotic and protic solvents could work together to stabilize both the NC surface and ligand shell.

These two possible modes of solvation were further studied using QM/MM simulations and the calculation results are shown in Figure 7. As anticipated, when the DMSO concentration was 10% in our QM/MM simulation, DMSO molecules were mainly found in surface cleft regions (Figure 7a) whereas water molecules were found at all locations on the surface of Na<sub>4</sub>Ag<sub>44</sub>(*p*-MBA)<sub>30</sub> (Figure 7b), indicating

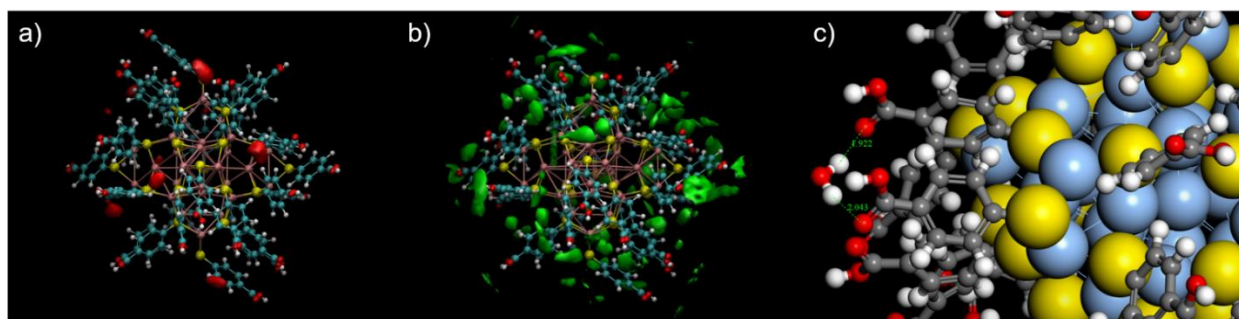


**Figure 7.** QM/MM simulations showing a) the distribution of DMSO (red cloud), b) H<sub>2</sub>O (green cloud) around Na<sub>4</sub>Ag<sub>44</sub>(*p*-MBA)<sub>30</sub> (pink – Ag, yellow – S, cyan – C, red – O, white – H), and c) interactions between H<sub>2</sub>O and carboxylate residues in 10% DMSO.

a favorable interaction between DMSO and surface Ag atoms. The radial distribution plot of the distances between DMSO oxygen atoms and surface Ag atoms consists of only one dominant peak at ~3 Å, as shown in Figure 8. This indicates both that DMSO selectively partitions to the surface of Na<sub>4</sub>Ag<sub>44</sub>(*p*-MBA)<sub>30</sub> and that the oxygen atoms are the coordinating residue, given the strong orientation preference. Compared to the pure DMSO system, the first Ag-O peak is shifted by ~0.2 Å and broadened for the 10% DMSO system (Figure 8). This shift and broadening would suggest



there is some competition between water and DMSO molecules at the Ag NC surface. Nevertheless, the absence of a second solvation shell (around 4.5 Å) for the 10% DMSO system indicates that DMSO is indeed more favored at the surface and that water molecules occupy the space around the NC where solvent-ligand interactions are more dominant.

QM/MM simulations also provide information on the response of the  $\text{Na}_4\text{Ag}_{44}(\text{p-MBA})_{30}$  structure to solvent coordination. From these simulation results, we found that Ag-Ag bonding increased on average by  $\sim 0.03$  Å (Figure S6) when the amount of coordinating DMSO was decreased from 100% to 10%. This is consistent with our EXAFS results (Table 3) and further supports our findings on the effects of solvent coordination. Lastly, we note that indeed water molecules were found to form hydrogen bonding interactions between the carboxylate groups of *p*-MBA ligands (Figure 7c), confirming that two modes of solvation from aprotic and protic

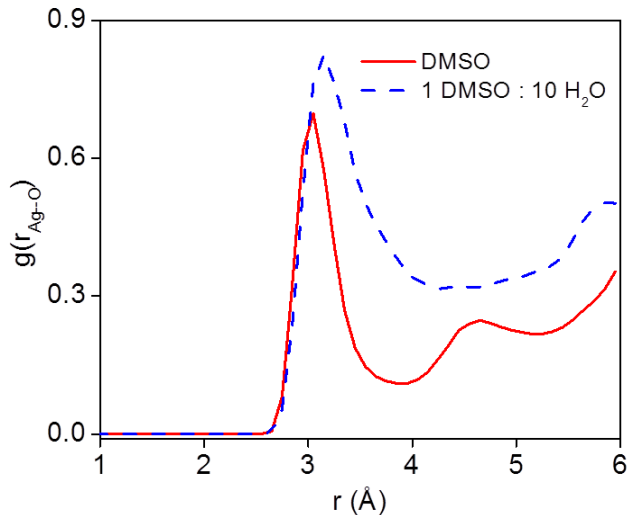


**Figure 8.** Radial distribution plots of sulfoxide distances to Ag atoms on NC surface for 100% DMSO and 10% DMSO systems obtained from QM/MM calculations.

solvents contribute to the stabilization of  $\text{Na}_4\text{Ag}_{44}(\text{p-MBA})_{30}$ . This notion is well in line with the observation in Figure 6 where the relative intensity of Ag-S WT-EXAFS domain increases after water is added. Addition of water can stabilize ligand bundling by H-bonding which strengthen the Ag-S interactions at the cluster surface, resulting in more rigid Ag-S framework and thus stronger feature in the WT-EXAFS.

## CONCLUSION

Solution-phase X-ray absorption spectroscopy experiments and quantum mechanics / molecular mechanics simulations were jointly employed to uncover how coordinating solvents interact with ultrastable  $\text{Na}_4\text{Ag}_{44}(\text{p-MBA})_{30}$  nanoclusters at the atomic scale. These results indicate that strongly coordinating molecules such as DMSO and DMF directly interact with Ag atoms on the surface of  $\text{Na}_4\text{Ag}_{44}(\text{p-MBA})_{30}$  particularly between ligand bundles and lead to contraction of the Ag core and variation of the S-Ag bonding properties. In addition, DMSO was found to coordinate with  $\text{Na}_4\text{Ag}_{44}(\text{p-MBA})_{30}$  via a sulfoxide-Ag interaction and was preferentially located on the Ag surface between ligand bundles, which could provide a secondary mechanism of steric stabilization. Furthermore, water was used as a co-solvent to illustrate that coordinating solvents and semi-aqueous conditions play an important role in protecting exposed surface regions and can further tailor the local structure of the silver nanocluster. Under the co-solvation conditions, aprotic coordinating solvent molecules preferentially interact with the surface silver while water molecules interact with ligands. Ligand bundling persisted across the varied solvation conditions. This work provides an atomic scale mechanism for the ultrahigh stability of  $\text{Na}_4\text{Ag}_{44}(\text{p-MBA})_{30}$  from the nanocluster-solvent interaction perspective and demonstrates the physical and electronic effects of coordinating solvents on  $\text{Na}_4\text{Ag}_{44}(\text{p-MBA})_{30}$  nanoclusters. This work may also provide guidelines for the development of synthetic strategies where the choice of solvent type may

influence the surface accessibility, the electronic properties, and ultimately, the stability of metal NCs, particularly for less inert metals. Furthermore, this level of information on solvent-nanocluster interactions could play an important role in the development of metal nanocluster-based technologies, such as biosensors and catalysts.

## MATERIALS AND METHODS

$\text{Na}_4\text{Ag}_{44}(\text{p-MBA})_{30}$  NCs were synthesized according to the protocol published by Desiredy *et al.*<sup>12</sup> Pertaining to this study, the reaction mixture used a water- dimethyl sulfoxide (DMSO) co-solvent and the final product was precipitated using dimethylformamide (DMF).

Ag K-edge XAFS data was collected for  $\text{Na}_4\text{Ag}_{44}(\text{p-MBA})_{30}$  NC samples from the CLS@APS beamline (Sector 20-BM) at the Advanced Photon Source (operating at 7.0 GeV). Both solid- and solution-phase measurements were conducted at 300 K and atmospheric pressure. The powdered sample collected at 90 K for the initial multi-shell fitting analysis was loaded into a helium-cooled cryostat chamber for measurement.  $\text{Na}_4\text{Ag}_{44}(\text{p-MBA})_{30}$  NCs for solid-phase samples were prepared by dissolving clusters in a small amount of DMF or DMSO (20 mg of NCs in 100  $\mu\text{L}$  solvent) and drop-casting them onto Kapton film. The concentrated drops were left to dry under  $\text{N}_2$  for at least one hour and then folded until an absorption of at least 0.5 was achieved. Solution-phase samples were prepared using a  $\sim 10$  mM solution of  $\text{Na}_4\text{Ag}_{44}(\text{p-MBA})_{30}$  NCs and utilizing a Teflon liquid cell with Kapton windows (designed and constructed at the CLS@APS beamline).

The amplitude reduction factor ( $S_0^2$ ) was fixed at 0.90 for Ag K-edge extended X-ray absorption fine structure (EXAFS) fitting, which was determined by fitting the Ag-Ag scattering of a Ag foil reference with a fixed Ag-Ag coordination number (CN) of 12. For multi-shell EXAFS fitting, CNs were fixed according to the  $\text{Na}_4\text{Ag}_{44}(\text{p-MBA})_{30}$  crystal structure. Theoretical phase-shifts and

scattering amplitudes for Ag-S and Ag-Ag scattering paths were calculated using the atomic coordinates from the  $\text{Na}_4\text{Ag}_{44}(\text{p-MBA})_{30}$  crystal structure model. A  $k$ -range of 3 to 12  $\text{\AA}^{-1}$  was used for the Fourier transformation (FT) to  $R$ -space. A fitting window of 1.5 to 3.5  $\text{\AA}$  was used for fits. Reported uncertainties for EXAFS fitting results were computed from off-diagonal elements of the correlation matrix, which were weighted by the square root of the reduced chi-squared value obtained from each simulated fit. The amount of experimental noise was also taken into consideration for each Fourier transformed  $R$ -space spectrum from 15–25  $\text{\AA}$ .<sup>27</sup> S K-edge X-ray absorption near edge structure (XANES) data were collected from the SXRMB beamline at the Canadian Light Source (operating at 2.9 GeV). Powdered samples were measured in fluorescence mode under room temperature and vacuum conditions. All samples were mounted onto a copper sample holder using carbon tape. Liquid-phase measurements were conducted in fluorescence mode using a Teflon liquid cell with a mylar measurement window. Wavelet transformed (WT)-EXAFS plots were generated using Morlet-type wavelets and a  $k$ -range of 3 to 12  $\text{\AA}^{-1}$  for all the samples.<sup>28</sup> To closely compare the WT-EXAFS of the samples, all the data processing parameters were kept the same except for the 90 K sample whose WT-EXAFS was not compared with other samples.

Quantum mechanical/molecular mechanical (QM/MM) molecular dynamics (MD) simulations were performed to investigate the influence of the different solvents on the structure of a Ag NC. The initial structure of  $[\text{Ag}_{44}(\text{p-MBA})_{30}]^{4-}$  was taken from the X-ray crystallography data,<sup>12</sup> and then solvated in two types of solvent environments: 1) pure solvent of 1514 DMSO molecules and 2) a co-solvent of 265 DMSO and 2651 water molecules. Four  $\text{Na}^+$  ions were added to balance the charge.

The solvated systems were simulated with periodic boundary conditions and were first equilibrated with classical MD (CMD) for 50 ns using the NPT ensemble ( $T = 300$  K,  $P = 1$  atm) with the time step of 1 fs, using the Amber 18 package,<sup>29</sup> and the GAFF,<sup>30</sup> FF14SB,<sup>31</sup> and TIP3P force-fields.<sup>32</sup> The positions of the Ag atoms were fixed during CMD simulations since our goal was to equilibrate the solvation structure. The atomic charges in  $[\text{Ag}_{44}(\text{p-MBA})_{30}]^{4-}$  were derived from fitting the restrained electrostatic potential (RESP) using CP2K.<sup>33</sup> Representative snapshots of the solvated systems after pre-equilibration CMD were then used in the QM/MM simulations. The energies of the QM region containing the  $[\text{Ag}_{44}(\text{p-MBA})_{30}]^{4-}$  cluster and the solvents in the first solvation shell were computed using the Quickstep module of CP2K, while the MM regions containing the remaining solvents were treated using the FIST module of CP2K with the same force field as in the CMD simulations. The QM regions were described with the mixed Gaussian and plane wave (GPW) approach using the Perdew-Burke-Ernzerhof (PBE) functional,<sup>34</sup> and the MOLOPT basis set with a double- $\zeta$  Gaussian basis set augmented with a set of p-type polarization functions (DZVP).<sup>35</sup> Plane waves were expanded up to a density cutoff of 400 Ry and used in conjunction with the GTH pseudopotentials to describe the core electrons.<sup>36–38</sup> The convergence threshold of the electronic structure relaxation was set to  $10^{-6}$  Hartree. We also employed the dispersion corrections in the QM calculations.<sup>39</sup> Six Gaussian functions were used for the Gaussian expansion of the electrostatic Potential (GEEP) to couple the QM and MM regions.<sup>40,41</sup> The QM simulation cell was cubic with a length of 30 Å. The periodicity was applied only to the MM simulation cell of 57 Å in length for pure DMSO and 50 Å in length for water-DMSO; the QM images were decoupled using the wavelet scheme.<sup>42,43</sup> The QM/MM simulations were carried out using the NVT ensemble at 300 K for about 15 ps, with the last half of the trajectories being used for analysis.

## ASSOCIATED CONTENT

**Supporting Information.** Ag K-edge EXAFS data for all samples presented in k-space, Fourier transformed R-space with fitted scattering paths and XANES spectra. Radial distribution plots for various interaction distances between sulfoxide residues, Ag atoms and thiolate S atoms. This material is available free of charge via the Internet at <http://pubs.acs.org>.

## AUTHOR INFORMATION

Corresponding Author

\* [peng.zhang@dal.ca](mailto:peng.zhang@dal.ca)

## Present Addresses

† Biosciences and Biotechnologies Institute of Aix-Marseille, CEA Cadarache, 13108 St. Paul  
lez Durance, France

## Author Contributions

The manuscript was written through contributions of all authors. All authors have given approval to the manuscript.

## ACKNOWLEDGMENT

D.M.C. would like to thank NSERC for financial support through the Alexander Graham Bell Canada Graduate Scholarship. P.Z. acknowledges funding support by NSERC. B.E.C. would like to thank the IPMI for financial support through an IPMI graduate fellowship. T.P.B. thanks the National Science Foundation for financial support (grants #0955148 and #1905262). The simulation work (B.L. and D.J.) was sponsored by the U.S. Department of Energy, Office of Science, Office of Basic Energy Sciences, Chemical Sciences, Geosciences, and Biosciences Division. This research used resources of the Advanced Photon Source, an Office of Science User Facility operated for the US Department of Energy (DOE) Office of Science by Argonne National Laboratory, and was supported by the US DOE under contract no. DE-AC02-06CH11357, and the Canadian Light Source (CLS) and its funding partners. The simulation work used resources of the National Energy Research Scientific Computing Center, a DOE Office of Science User Facility supported by the Office of Science of the U.S. Department of Energy under contract no. DE-AC02-05CH11231.

## REFERENCES

- (1) Jain, P. K.; Huang, X.; El-Sayed, I. H.; El-Sayed, M. A. Noble Metals on the Nanoscale: Optical and Photothermal Properties and Some Applications in Imaging, Sensing, Biology, and Medicine. *Acc. Chem. Res.* **2008**, *41*, 1578–1586.
- (2) Kang, S. Y.; Kim, K. Comparative Study of Dodecanethiol-Derivatized Silver Nanoparticles Prepared in One-Phase and Two-Phase Systems. *Langmuir* **1998**, *14*, 226–230.
- (3) Kumar, S.; Bolan, M. D.; Bigioni, T. P. Glutathione-Stabilized Magic-Number Silver Cluster Compounds. *J. Am. Chem. Soc.* **2010**, *132*, 13141–13143.
- (4) He, S.; Yao, J.; Jiang, P.; Shi, D.; Zhang, H.; Xie, S.; Pang, S.; Gao, H. Formation of Silver Nanoparticles and Self-Assembled Two-Dimensional Ordered Superlattice. *Langmuir* **2001**, *17*, 1571–1575.
- (5) Jadzinsky, P. D.; Calero, G.; Ackerson, C. J.; Bushnell, D. A.; Kornberg, R. D. Structure of

- a Thiol Monolayer-Protected Gold Nanoparticle at 1.1 Å Resolution. *Science* **2007**, *318*, 430–433.
- (6) Rai, M.; Yadav, A.; Gade, A. Silver Nanoparticles as a New Generation of Antimicrobials. *Biotechnol. Adv.* **2009**, *27*, 76–83.
  - (7) Standridge, S. D.; Schatz, G. C.; Hupp, J. T.; Standridge, S. D.; Schatz, G. C.; Hupp, J. T. Toward Plasmonic Solar Cells: Protection of Silver Nanoparticles via Atomic Layer Deposition of TiO<sub>2</sub>. *Langmuir* **2009**, *25*, 2596–2600.
  - (8) McMahon, M. D.; Lopez, R.; Meyer, H. M.; Feldman, L. C.; Haglund, R. F. Rapid Tarnishing of Silver Nanoparticles in Ambient Laboratory Air. *Appl. Phys. B Lasers Opt.* **2005**, *80*, 915–921.
  - (9) Yang, J.; Jin, R. New Advances in Atomically Precise Silver Nanoclusters. *ACS Mater. Lett.* **2019**, *1*, 482–489.
  - (10) Bhattarai, B.; Zaker, Y.; Atnagulov, A.; Yoon, B.; Landman, U.; Bigioni, T. P. Chemistry and Structure of Silver Molecular Nanoparticles. *Acc. Chem. Res.* **2018**, *51*, 3104–3113.
  - (11) Yang, H.; Wang, Y.; Huang, H.; Gell, L.; Lehtovaara, L.; Malola, S.; Häkkinen, H.; Zheng, N. All-Thiol-Stabilized Ag<sub>44</sub> and Au<sub>12</sub>Ag<sub>32</sub> Nanoparticles with Single-Crystal Structures. *Nat. Commun.* **2013**, *4*, 2422.
  - (12) Desiredy, A.; Conn, B. E.; Guo, J.; Yoon, B.; Barnett, R. N.; Monahan, B. M.; Kirschbaum, K.; Griffith, W. P.; Whetten, R. L.; Landman, U.; et al. Ultrastable Silver Nanoparticles. *Nature* **2013**, *501*, 399–402.
  - (13) Conn, B. E.; Desiredy, A.; Atnagulov, A.; Wickramasinghe, S.; Bhattarai, B.; Yoon, B.; Barnett, R. N.; Abdollahian, Y.; Kim, Y. W.; Griffith, W. P.; et al. M<sub>4</sub>Ag<sub>44</sub>(p-MBA)<sub>30</sub> Molecular Nanoparticles. *J. Phys. Chem. C* **2015**, *119*, 11238–11249.
  - (14) Urushizaki, M.; Kitazawa, H.; Takano, S.; Takahata, R.; Yamazoe, S.; Tsukuda, T. Synthesis and Catalytic Application of Ag<sub>44</sub> Clusters Supported on Mesoporous Carbon. *J. Phys. Chem. C* **2015**, *119*, 27483–27488.
  - (15) Bakr, O. M.; Amendola, V.; Aikens, C. M.; Wenseleers, W.; Li, R.; Dal Negro, L.; Schatz, G. C.; Stellacci, F. Silver Nanoparticles with Broad Multiband Linear Optical Absorption. *Angew. Chemie* **2009**, *121*, 6035–6040.
  - (16) Luedtke, W. D.; Landman, U. Structure, Dynamics, and Thermodynamics of Passivated Gold Nanocrystallites and Their Assemblies. *J. Phys. Chem.* **1996**, *100*, 13323–13329.
  - (17) Conn, B. E.; Atnagulov, A.; Bhattarai, B.; Yoon, B.; Landman, U.; Bigioni, T. P. Synthetic and Postsynthetic Chemistry of M<sub>4</sub>AuxAg<sub>44-x</sub>(p-MBA)<sub>30</sub> Alloy Nanoparticles. *J. Phys. Chem. C* **2018**, *122*, 13166–13174.
  - (18) Wan, X.-K.; Wang, J.-Q.; Nan, Z.-A.; Wang, Q.-M. Ligand Effects in Catalysis by Atomically Precise Gold Nanoclusters. *Sci. Adv.* **2017**, *3*, e1701823.



- (19) Dufour, F.; Fresch, B.; Purupthy, O.; Cheneac, C.; Remacle, F. Ligand and Solvation Effects on the Structural and Electronic Properties of Small Gold Clusters. *J. Phys. Chem. C* **2014**, *118*, 4362–4376.
- (20) Kim, A.; Zeng, C.; Zhou, M.; Jin, R. Surface Engineering of Au<sub>36</sub>(SR)<sub>24</sub> Nanoclusters for Photoluminescence Enhancement. *Part. Part. Syst. Charact.* **2017**, *34*, 1600388.
- (21) Chevrier, D. M.; Raich, L.; Rovira, C.; Das, A.; Luo, Z.; Yao, Q.; Chatt, A.; Xie, J.; Jin, R.; Akola, J.; et al. Molecular-Scale Ligand Effects in Small Gold–Thiolate Nanoclusters. *J. Am. Chem. Soc.* **2018**, *140*, 15430–15436.
- (22) Conn, B. E.; Atnagulov, A.; Bhattarai, B.; Yoon, B.; Landman, U.; Bigioni, T. P. Synthetic and Postsynthetic Chemistry of M<sub>4</sub>AuxAg<sub>44–x</sub>(*p*-MBA)<sub>30</sub> Alloy Nanoparticles. *J. Phys. Chem. C* **2018**, *122*, 13166–13174.
- (23) MacDonald, M. A.; Zhang, P.; Qian, H.; Jin, R. Site-Specific and Size-Dependent Bonding of Compositionally Precise Gold–Thiolate Nanoparticles from X-Ray Spectroscopy. *J. Phys. Chem. Lett.* **2010**, *1*, 1821–1825.
- (24) Glaser, T.; Hedman, B.; Hodgson, K. O.; Solomon, E. I. Ligand K-Edge X-Ray Absorption Spectroscopy: A Direct Probe of Ligand–Metal Covalency. *Acc. Chem. Res.* **2000**, *33*, 859–868.
- (25) MacDonald, M. A.; Chevrier, D. M.; Zhang, P.; Qian, H.; Jin, R. The Structure and Bonding of Au<sub>25</sub>(SR)<sub>18</sub> Nanoclusters from EXAFS: The Interplay of Metallic and Molecular Behavior. *J. Phys. Chem. C* **2011**, *115*, 15282–15287.
- (26) Koivisto, J.; Chen, X.; Donnini, S.; Lahtinen, T.; Häkkinen, H.; Groenhof, G.; Pettersson, M. Acid–Base Properties and Surface Charge Distribution of the Water-Soluble Au<sub>102</sub>(*p*-MBA)<sub>44</sub> Nanocluster. *J. Phys. Chem. C* **2016**, *120*, 10041–10050.
- (27) Newville, M.; Boyanov, B. I.; Sayers, D. E. Estimation of Uncertainties in XAFS Data. *J. Synchrotron Radiat.* **1999**, *6*, 264–265.
- (28) Chevrier, D. M.; Raich, L.; Rovira, C.; Das, A.; Luo, Z.; Yao, Q.; Chatt, A.; Xie, J.; Jin, R.; Akola, J.; et al. Molecular-Scale Ligand Effects in Small Gold–Thiolate Nanoclusters. *J. Am. Chem. Soc.* **2018**, *140*, 15430–15436.
- (29) D.A. Case, I.Y. Ben-Shalom, S.R. Brozell, D.S. Cerutti, T.E. Cheatham, III, V.W.D. Cruzeiro, T.A. Darden, R.E. Duke, D. Ghoreishi, M.K. Gilson, H. Gohlke, A.W. Goetz, D. Greene, R Harris, N. Homeyer, S. Izadi, A. Kovalenko, T. Kurtzman, T.S. Lee, S. LeGra, D. M. Y. and P. A. K. AMBER 2018. University of California, San Francisco 2018.
- (30) Wang, J. M.; Wolf, R. M.; Caldwell, J. W.; Kollman, P. A.; Case, D. A. Development and Testing of a General Amber Force Field. *J. Comput. Chem.* **2004**, *25*, 1157.
- (31) Maier, J. A.; Martinez, C.; Kasavajhala, K.; Wickstrom, L.; Hauser, K. E.; Simmerling, C. Ffl4SB: Improving the Accuracy of Protein Side Chain and Backbone Parameters from Ff99SB. *J. Chem. Theory Comput.* **2015**, *11*, 3696–3713.

- (32) Jorgensen, W. L.; Chandrasekhar, J.; Madura, J. D.; Impey, R. W.; Klein, M. L. Comparison of Simple Potential Functions for Simulating Liquid Water. *J. Chem. Phys.* **1983**, *79*, 926.
- (33) Hutter, J.; Iannuzzi, M.; Schiffmann, F.; VandeVondele, J. Cp2k: Atomistic Simulations of Condensed Matter Systems. *Wiley Interdiscip. Rev. Comput. Mol. Sci.* **2014**, *4*, 15–25.
- (34) Perdew, J.; Burke, K.; Ernzerhof, M. Generalized Gradient Approximation Made Simple. *Phys. Rev. Lett.* **1996**, *77*, 3865–3868.
- (35) VandeVondele, J.; Hutter, J. Gaussian Basis Sets for Accurate Calculations on Molecular Systems in Gas and Condensed Phases. *J. Chem. Phys.* **2007**, *127*, 114105.
- (36) Goedecker, S.; Teter, M.; Hutter, J. Separable Dual-Space Gaussian Pseudopotentials. *Phys. Rev. B* **1996**, *54*, 1703–1710.
- (37) Hartwigsen, C.; Goedecker, S.; Hutter, J. Relativistic Separable Dual-Space Gaussian Pseudopotentials from H to Rn. *Phys. Rev. B* **1998**, *58*, 3641–3662.
- (38) Krack, M. Pseudopotentials for H to Kr Optimized for Gradient-Corrected Exchange-Correlation Functionals. *Theor. Chem. Acc.* **2005**, *114*, 145–152.
- (39) Grimme, S.; Antony, J.; Ehrlich, S.; Krieg, H. A Consistent and Accurate Ab Initio Parametrization of Density Functional Dispersion Correction (DFT-D) for the 94 Elements H-Pu. *J. Chem. Phys.* **2010**, *132*, 154104.
- (40) Laino, T.; Mohamed, F.; Laio, A.; Parrinello, M. An Efficient Real Space Multigrid QM/MM Electrostatic Coupling. *J. Chem. Theory Comput.* **2005**, *1*, 1176–1184.
- (41) Laino, T.; Mohamed, F.; Laio, A.; Parrinello, M. An Efficient Linear-Scaling Electrostatic Coupling for Treating Periodic Boundary Conditions in QM/MM Simulations. *J. Chem. Theory Comput.* **2006**, *2*, 1370–1378.
- (42) Genovese, L.; Deutsch, T.; Neelov, A.; Goedecker, S.; Beylkin, G. Efficient Solution of Poisson's Equation with Free Boundary Conditions. *J. Chem. Phys.* **2006**, *125*, 74105.
- (43) Genovese, L.; Deutsch, T.; Goedecker, S. Efficient and Accurate Three-Dimensional Poisson Solver for Surface Problems. *J. Chem. Phys.* **2007**, *127*, 54704.

# Supporting Information:

## **Interactions between Ultrastable Na<sub>4</sub>Ag<sub>44</sub>(SR)<sub>30</sub> Nanoclusters and Coordinating Solvents: Uncovering the Atomic-scale Mechanism**

*Daniel M. Chevrier,<sup>1,†</sup> Brian E. Conn,<sup>2</sup> Bo Li,<sup>3</sup> De-en Jiang,<sup>3</sup> Terry P. Bigioni,<sup>2</sup> Amares Chatt,<sup>1</sup> Peng Zhang<sup>\*l</sup>*

<sup>1</sup>Department of Chemistry, Dalhousie University, Halifax, NS B3H 4J3, Canada

<sup>2</sup>Department of Chemistry and Biochemistry, University of Toledo, Toledo, Ohio 43606, United States

<sup>3</sup>Department of Chemistry, University of California, Riverside, California 92521, United States

\*Corresponding Author: peng.zhang@dal.ca

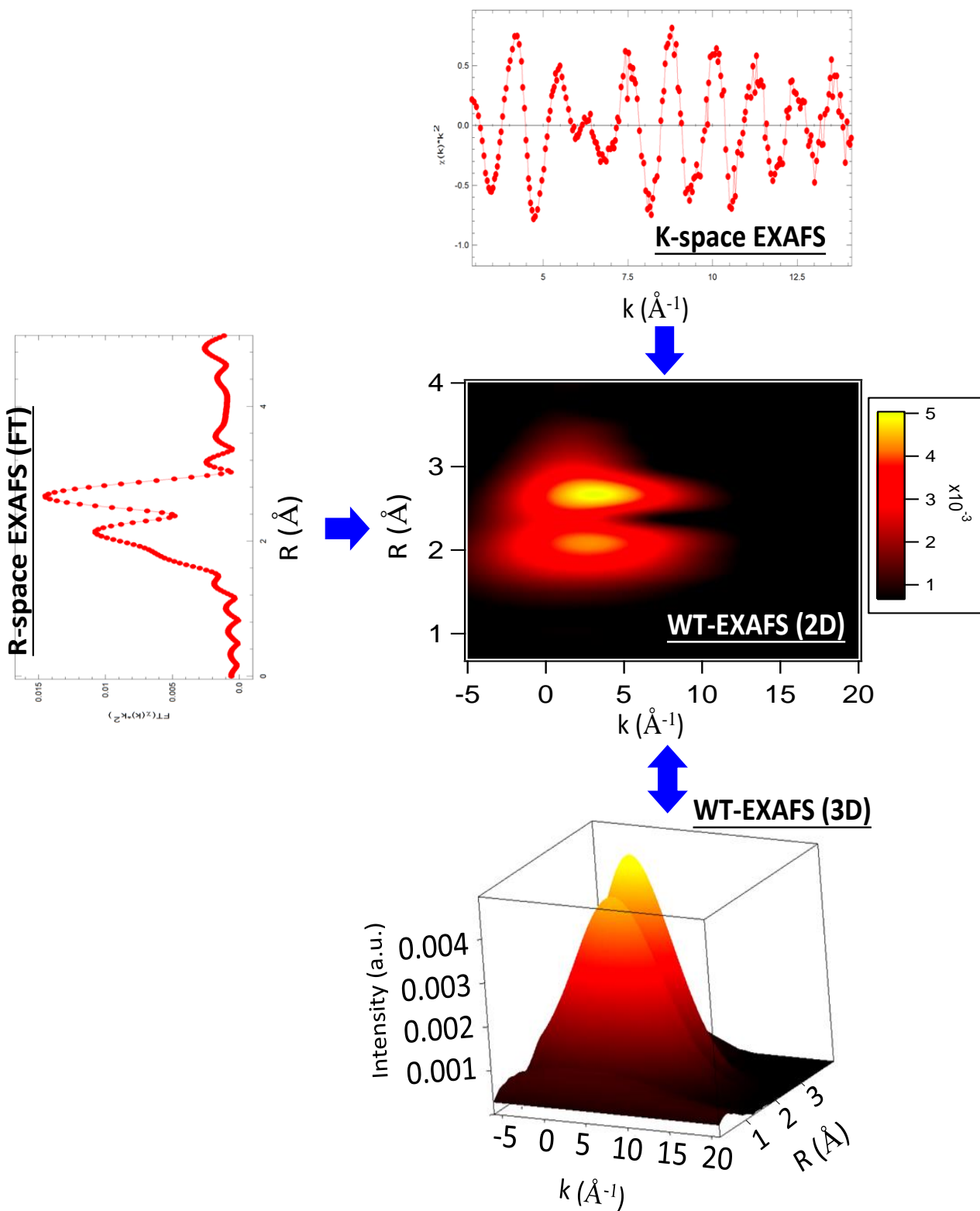


**Figure S1.** Demonstration of the relationship between the WT-EXAFS, the k-space and R-space EXAFS. Both the 2D WT-EXAFS of  $\text{Na}_4\text{Ag}_{44}(\text{SR})_{30}$  (90K) and its conversion to a 3D plot are shown.

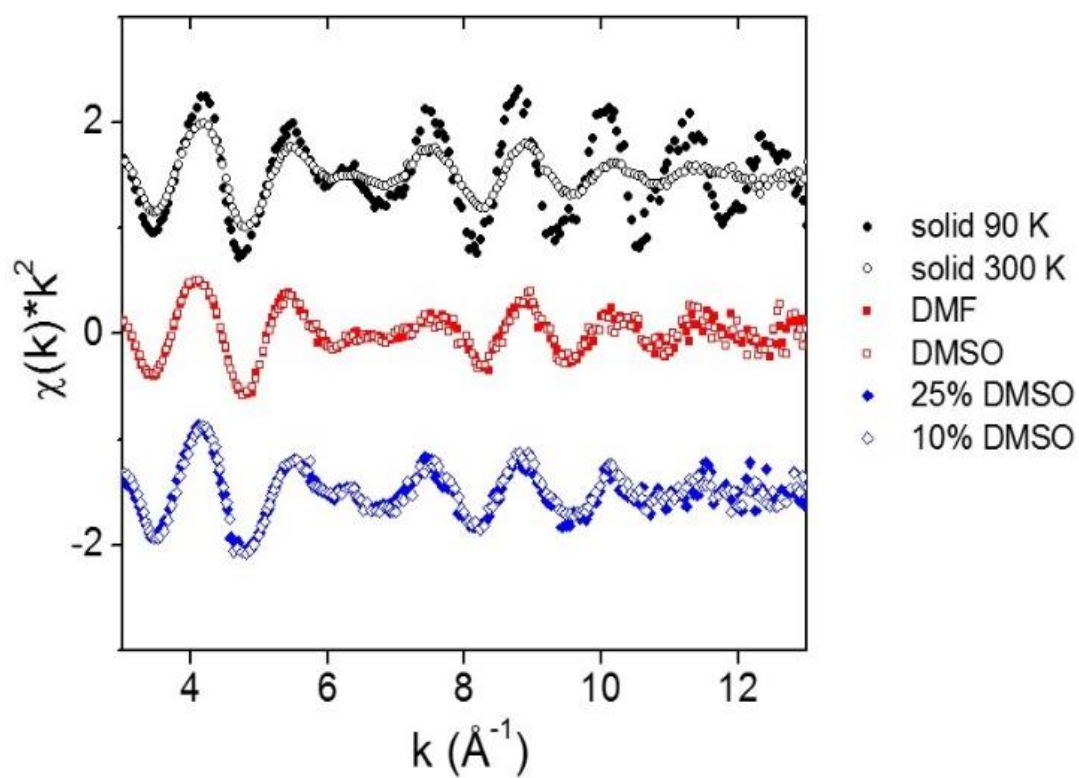


**Figure S2.** Ag K-edge  $k$ -space spectra of  $\text{Na}_4\text{Ag}_{44}(\text{p-MBA})_{30}$  NCs at various temperatures in the solid-phase and under solution-phase conditions.

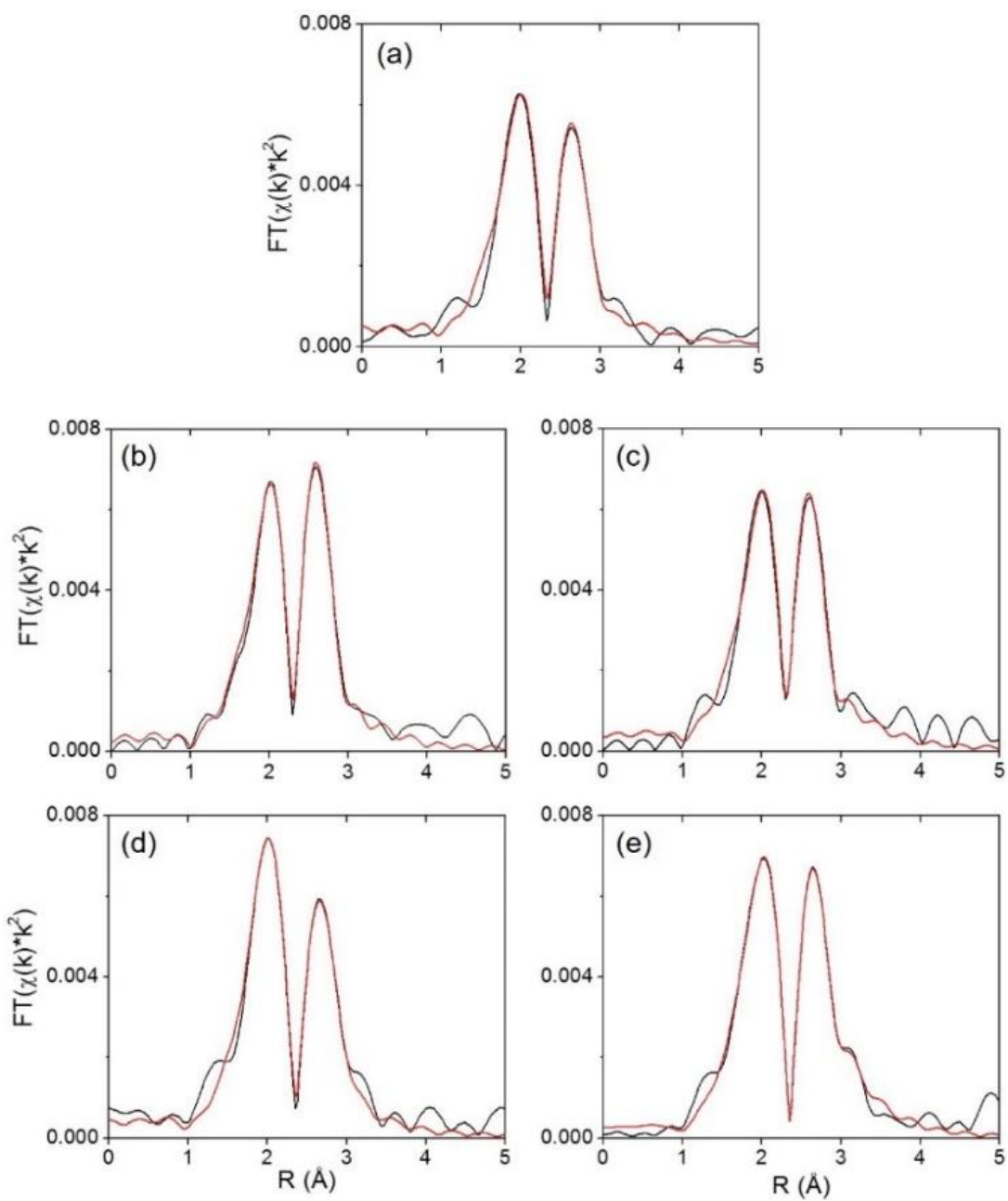


**Figure S3.** Ag K-edge EXAFS (black line) and multi-shell fit (red line) of  $\text{Na}_4\text{Ag}_{44}(\text{p-MBA})_{30}$  NCs in (a) solid-phase (300 K), (b) DMF, (c) DMSO, (d) 25% DMSO in water and (e) 10% DMSO in water.

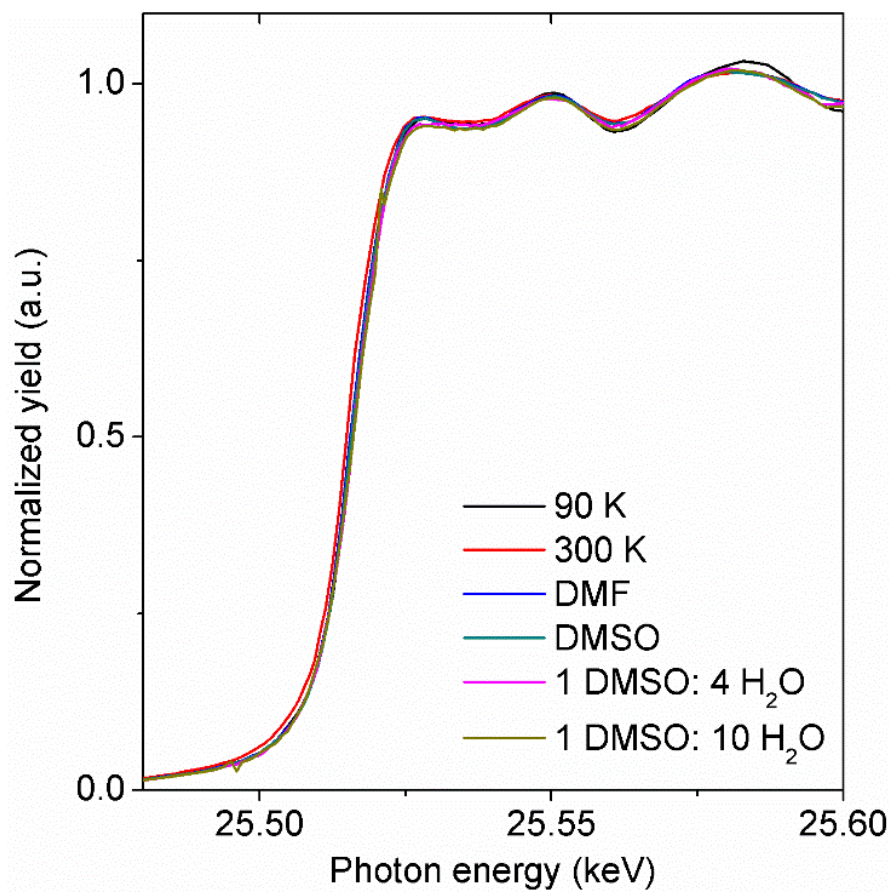


**Figure S4.** Ag K-edge XANES spectra of  $\text{Na}_4\text{Ag}_{44}(\text{p-MBA})_{30}$  NCs at various temperatures in the solid-phase and under solution-phase conditions.

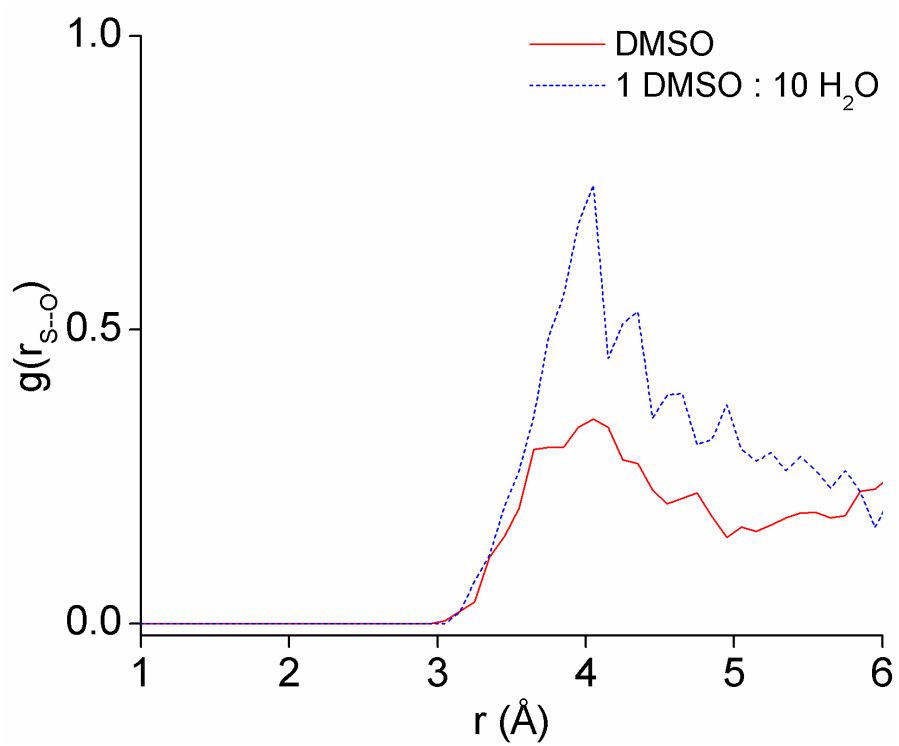


**Figure S5.** Radial distribution plot sulfoxide distances to S atoms of p-MBA ligands within Na<sub>4</sub>Ag<sub>44</sub>(p-MBA)<sub>30</sub> from QM/MM calculations.



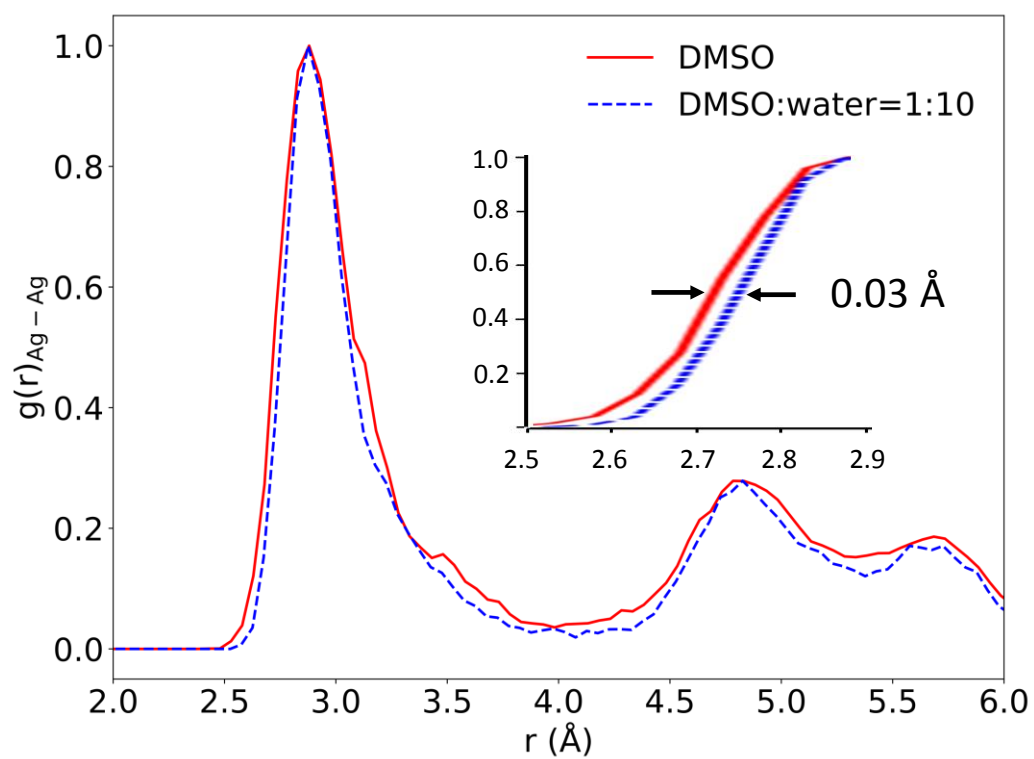


**Figure S6.** Radial distribution plot of Ag-Ag bond distances within  $\text{Na}_4\text{Ag}_{44}(\text{p-MBA})_{30}$  from QM/MM calculations. The inset is a close comparison of the half peak maximum position of the two samples with a shift of ca. 0.03 Å.